Supporting information

Modulating local pH environment in ZnO-Ce_x catalysts for efficient neutral H_2O_2 electrosynthesis

Yuxiang Zhang [a, b], Zibo Geng [a], Hao Zheng [a], Yue Lu [a], Xinyu Shan [a], Xinxian Zhu [a], Shan Ding [a]*

[a] Anhui Province Key Laboratory of Conservation and Utilization for Dabie Mountain Special Bio-Resources, West Anhui University, Lu'an, 237012, Anhui, China

[b] Key Laboratory for Soft Chemistry and Functional Materials (Ministry of Education), School of Chemistry and Chemical Engineering, Nanjing University of Science and Technology, Ministry of Education, Nanjing, 210094, China

*Corresponding e-mail: shan.ding@wxc.edu.cn (S.D.)

I. Experiment section

1. Physical characterizations

The morphology of the samples was examined with a ZEISS GeminiSEM 300 field-emission scanning electron microscope (SEM). Microstructural details were further analysed by transmission electron microscopy (TEM) and high-resolution TEM (HRTEM) using an FEI Talos F200X G2 instrument at an accelerating voltage of 300 kV. Crystal structure was determined by X-ray diffraction (XRD) on a Bruker D8 ADVANCE diffractometer with Cu Kα radiation (λ = 1.5418 Å), operating at 40 kV and 40 mA. Surface chemical composition and states were investigated by X-ray photoelectron spectroscopy (XPS) on a Thermo Scientific K-Alpha spectrometer (Al Kα source, 1486.6 eV), with survey scans ranging from 0 to 1400 eV. Fourier transform infrared (FT-IR) spectra were acquired using a Thermo Scientific Nicolet iS5 spectrophotometer, and ultraviolet-visible (UV-vis) absorption spectra were recorded on a TU-1950 spectrophotometer. *In situ* attenuated total reflection surface-enhanced infrared absorption spectroscopy (ATR-SEIRAS) were collected on a Bruker INVENIO instrument equipped with an accessory and a CHI1140C electrochemical workstation. All electrochemical tests were conducted in a standard three-electrode configuration using a CHI660E electrochemical workstation equipped with a high-current amplifier.

2. Electrochemical characterization using a rotating ring-disk electrode (RRDE)

All rotating ring-disk electrode (RRDE) measurements were carried out with a four-electrode electrochemical workstation (CHI 660E). The RRDE tip consisted of a glassy

carbon disk and a platinum ring. To prepare the working electrode, a catalyst ink was first formulated by ultrasonically dispersing 5 mg of catalyst for 1 hour in a mixture containing 750 μL isopropanol (99%), 210 μL deionized water, and 40 μL of 5 wt% Nafion solution. Then, 5 μL of the homogeneous ink was drop-cast onto the disk surface. A carbon rod and an Ag/AgCl electrode (saturated KCl) were used as the counter and reference electrodes, respectively. All measured potentials were converted to the reversible hydrogen electrode (RHE) scale using the equation:

$$E_{RHE} = E_{Ag/AgCl} + 0.059\ pH + 0.197$$

The oxygen reduction reaction (ORR) activity was assessed via linear sweep voltammetry (LSV) at a scan rate of 5 mV s^{-1} and a rotation speed of 1600 rpm to evaluate H_2O_2 production at the disk [1, 2]. Before data collection, the working electrode was stabilized by repeated potential cycling until a steady current response was obtained.

The H_2O_2 selectivity (%) was calculated by the following equation:

$$H_2O_2(\%) = \frac{2 \times \frac{i_r}{N}}{|i_d| + \frac{i_r}{N}} \times 100\%$$

The electron transfer number (n) was calculated by the following equation:

$$n = \frac{4 \times |i_d|}{|i_d| + i_r/N}$$

Where i_d and i_r denote the disk current and ring currents, respectively, and N represents the RRDE collection efficiency, which was experimentally determined to be 0.37.

3. Flow cell electrolysis and H_2O_2 quantification

The working electrode for flow cell experiments was prepared by spray-coating a catalyst ink onto a gas diffusion layer (GDL). The ink was obtained by ultrasonically dispersing 5 mg of catalyst and 50 μL of 5 wt% Nafion solution in 950 μL of isopropanol for one hour. The catalyst loading was controlled at 0.2 mg cm^{-2}. Electrochemical tests were conducted in a custom flow cell, with the catalyst-coated GDL as the working electrode, an IrO_2 plate as the counter electrode, and an Ag/AgCl electrode (saturated KCl) as the reference. The electrolyte in both compartments was 0.5 M K_2SO_4 solution.

The concentration of H_2O_2 produced at the cathode was quantified using a titanium sulfate colorimetric method [3, 4]. This assay is based on the formation of a yellow peroxotitanium complex, the absorbance of which at 408 nm was measured by UV-vis spectroscopy. The measured absorbance was correlated with a pre-established calibration curve (Fig. S2) to determine the H_2O_2 concentration.

The yield rate of H_2O_2 (Y, mol g_{cat}^{-1} h^{-1}) was calculated as follows:

$$Y = \frac{c(H_2O_2) \times V}{M \times t \times s \times m_{cat}}$$

The Faradaic efficiency (FE, %) was calculated as follows:

$$FE = \frac{2F \times c(H_2O_2) \times V}{34 \times \int_0^t Idt}$$

Where $c(H_2O_2)$ represents H_2O_2 concentration (mg L^{-1}), V is electrolyte volume (L), M denotes the molar mass of H_2O_2 (34 g mol^{-1}), m_{cat} is catalyst loading (mg cm^{-2}),

s is the electrode area (cm^2), F denotes the Faraday constant (96485 C mol^{-1}), the integral $\int_0^t Idt$ corresponds to the total charge passed, t is electrolysis time (h).

4. The measurement of local pHs by RRDE

Electrode potential exhibits pH sensitivity, thereby enabling the monitoring of pH variations at the working electrode surface [5-7]. In the present work, the pH at the catalyst surface was determined using the rotating ring-disk electrode (RRDE) technique. Specifically, the dependence of open-circuit potential (E_{oc}) on electrolyte pH was quantified via the ring electrode of the RRDE. The relationship between E_{oc} and the pH at the ring electrode is described by the following equation:

$$E_{oc} = a \times pH_{ring} + b \quad (1)$$

Where a and b are derived from the linear fitting of E_{oc} against pH. Subsequently, the pH values at the catalyst surface were measured under different applied potentials. Linear sweep voltammetry (LSV) measurements were conducted on the RRDE-supported catalyst in electrolytes of varying pH, with the open-circuit potential of the ring electrode recorded.

II. Supplementary Results

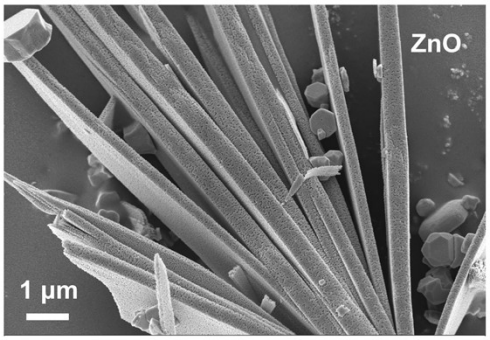

Figure S1 Scanning electron microscopy (SEM) image of ZnO.

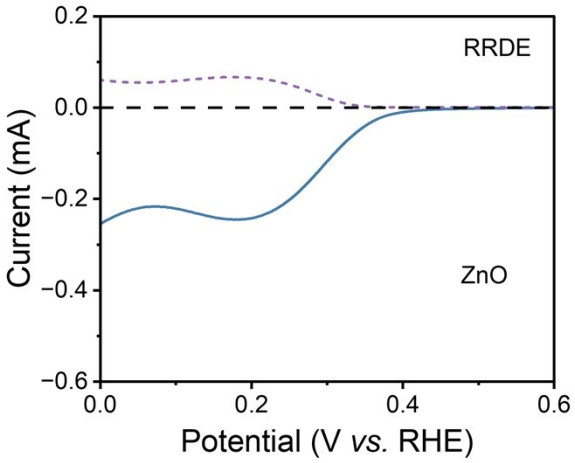

Figure S2 LSV of ZnO in 0.5 M K_2SO_4 by using RRDE.

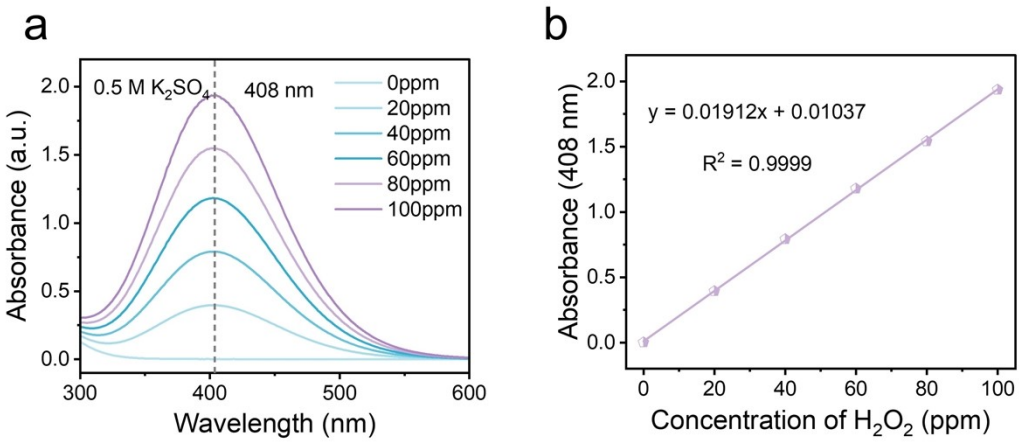

Figure S3 The calibration curve for hydrogen peroxide was measured by a traditional titration method in 0.5 M K_2SO_4 electrolyte. (a) The standard UV-Vis adsorption spectra of H_2TiO_4 with different H_2O_2 concentrations; (b) Calibration curve used for estimation of H_2O_2 concentrations.

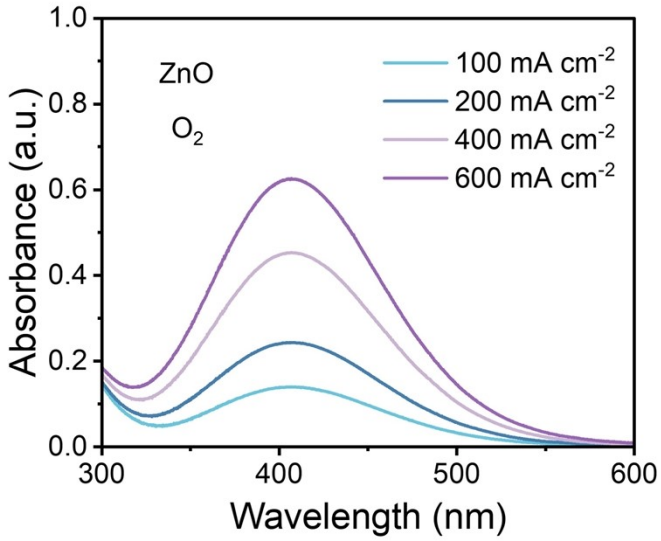

Figure S4 The UV-vis spectra under chronopotentiometry test at different current densities for ZnO.

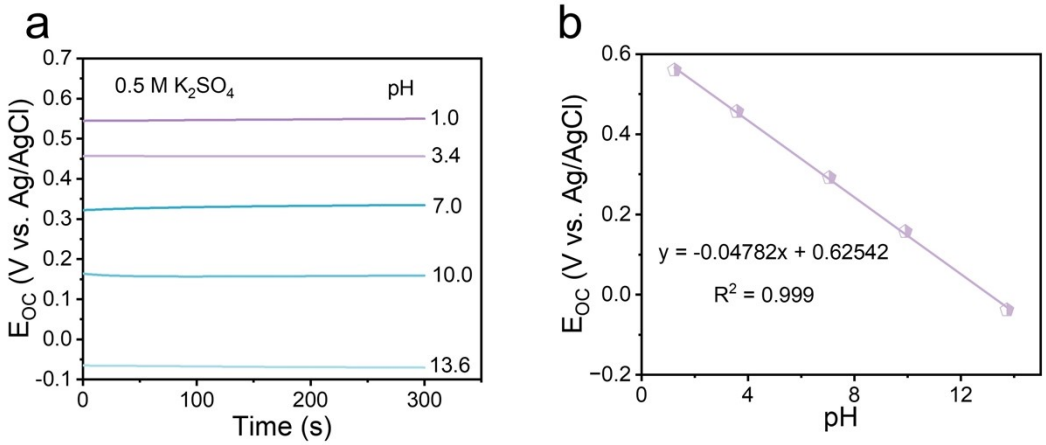

Figure S5 The calibration curves for local pHs by using RRDE. (a) Elapse time and (b) pH dependence of open circuit potential (E_{oc}) for Pt-ring electrode. The measurement was performed in K_2SO_4, and the pH of the electrolyte was changed by adding H_2SO_4 or KOH.

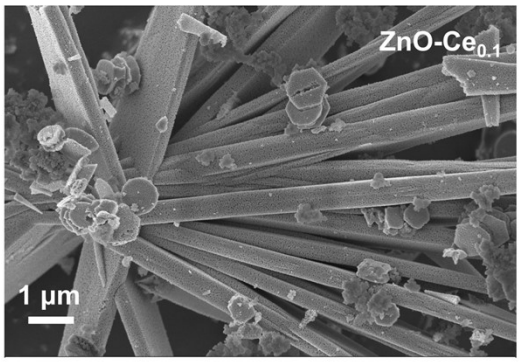

Figure S6 Scanning electron microscopy (SEM) image of ZnO-$Ce_{0.1}$.

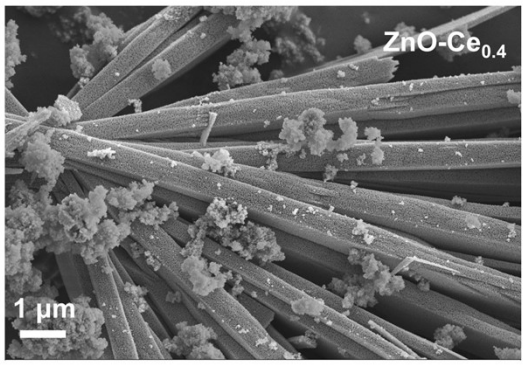

Figure S7 Scanning electron microscopy (SEM) image of ZnO-$Ce_{0.4}$.

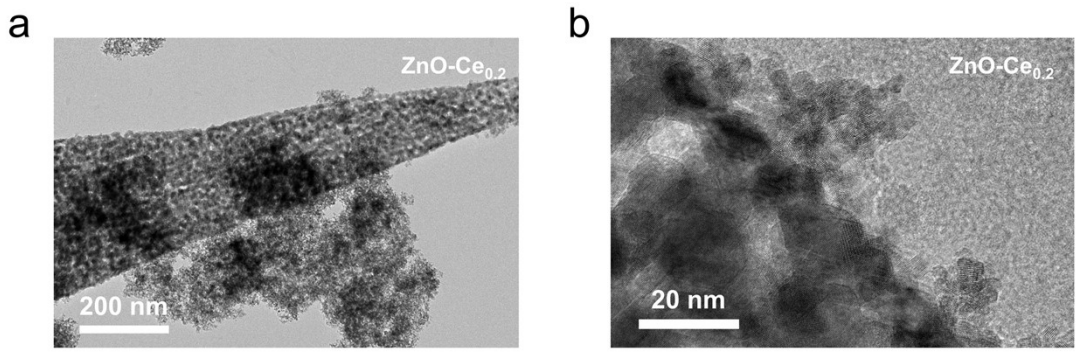

Figure S8 Transmission electron microscopy (TEM) images of ZnO-$Ce_{0.2}$ (scale bar: 200 nm for a; 20 nm for b).

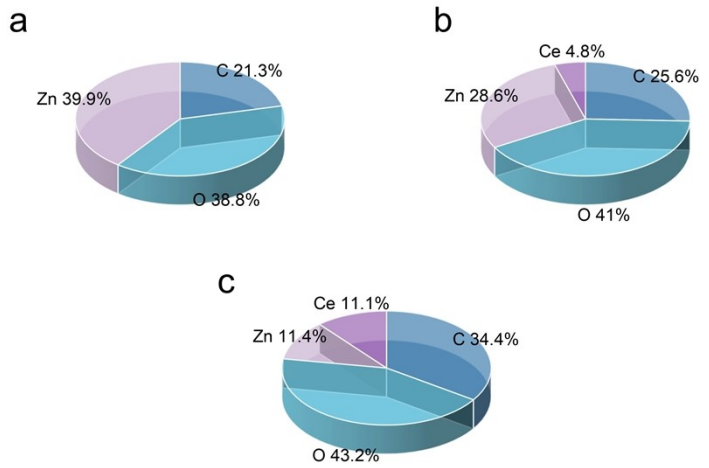

Figure S9 Charts showing the percentages of C, O, Zn and Ce elements by XPS results.

(a) ZnO; (b) ZnO-$Ce_{0.1}$ and (c) ZnO-$Ce_{0.4}$.

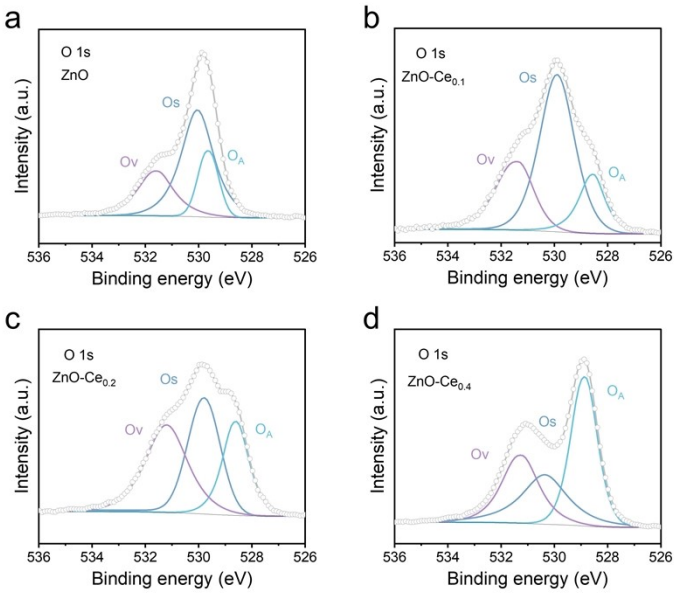

Figure S10 High-resolution XPS spectrums of O 1s. (a) ZnO; (b) ZnO-$Ce_{0.1}$; (c) ZnO-$Ce_{0.2}$ and (d) ZnO-$Ce_{0.4}$.

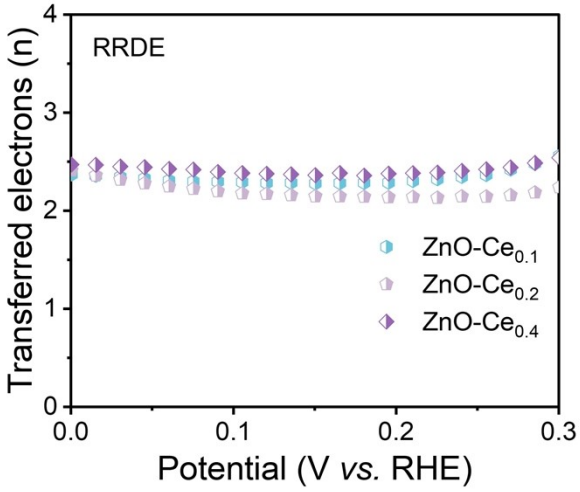

Figure S11 Electron transfer number (n) for ZnO-$Ce_{0.1}$, ZnO-$Ce_{0.2}$ and ZnO-$Ce_{0.4}$ tested in RRDE.

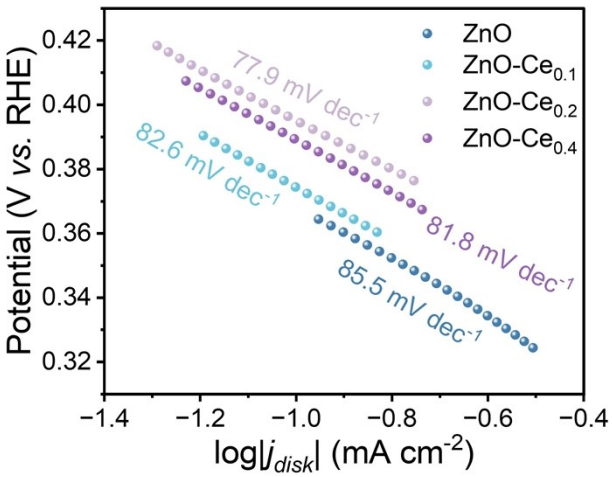

Figure S12 The Tafel slopes for ZnO, ZnO-$Ce_{0.1}$, ZnO-$Ce_{0.2}$ and ZnO-$Ce_{0.4}$.

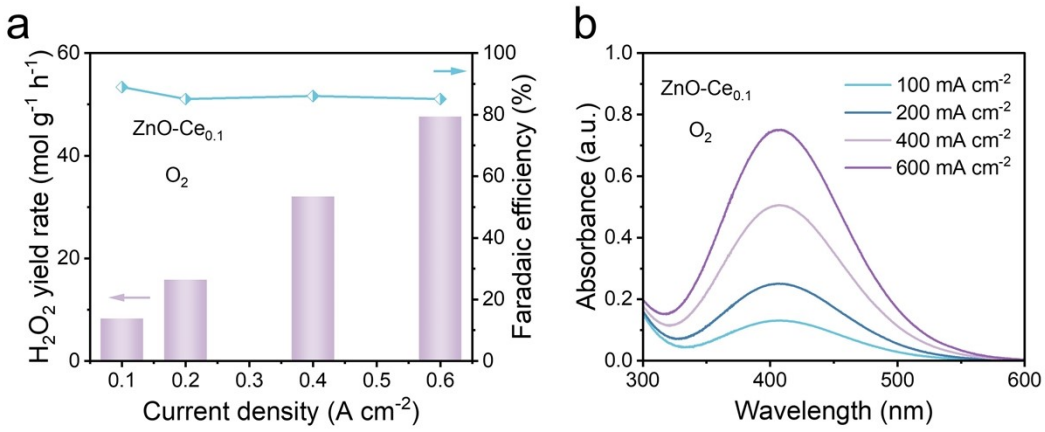

Figure S13 The $2e^-$ ORR performance of ZnO-$Ce_{0.1}$ in flow cell (under O_2). (a) The H_2O_2 yield rates and Faradaic efficiencies calculated by chronopotentiometry test; (b) The UV-vis spectra under chronopotentiometry test at different current densities.

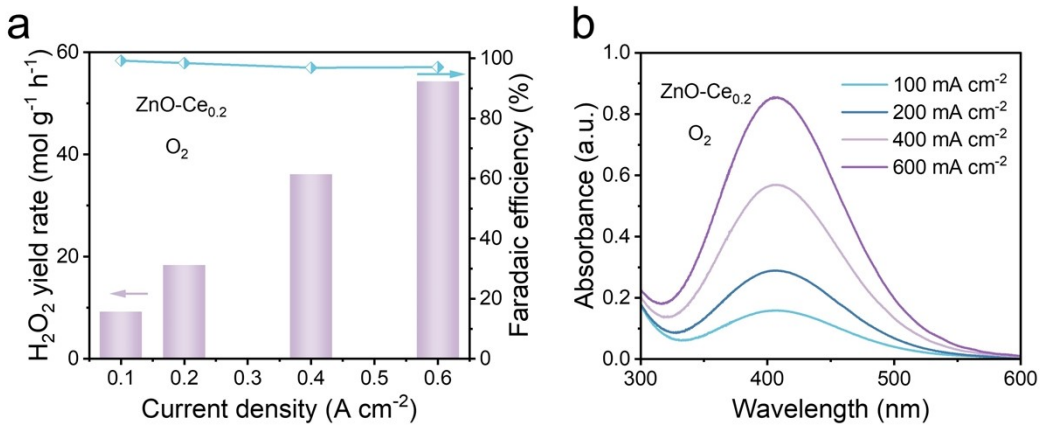

Figure S14 The $2e^-$ ORR performance of ZnO-$Ce_{0.2}$ in flow cell (under O_2). (a) The H_2O_2 yield rates and Faradaic efficiencies calculated by chronopotentiometry test; (b) The UV-vis spectra under chronopotentiometry test at different current densities.

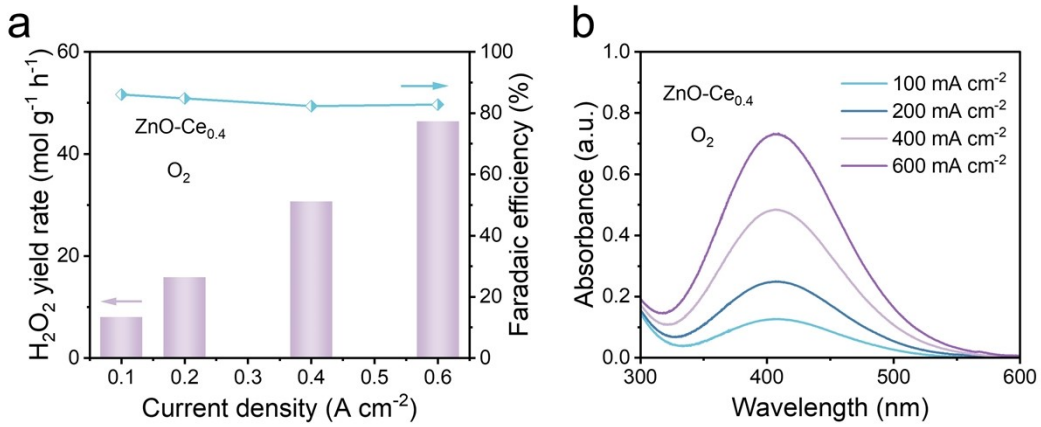

Figure S15 The $2e^-$ ORR performance of ZnO-$Ce_{0.4}$ in flow cell (under O_2). (a) The H_2O_2 yield rates and Faradaic efficiencies calculated by chronopotentiometry test; (b) The UV-vis spectra under chronopotentiometry test at different current densities.

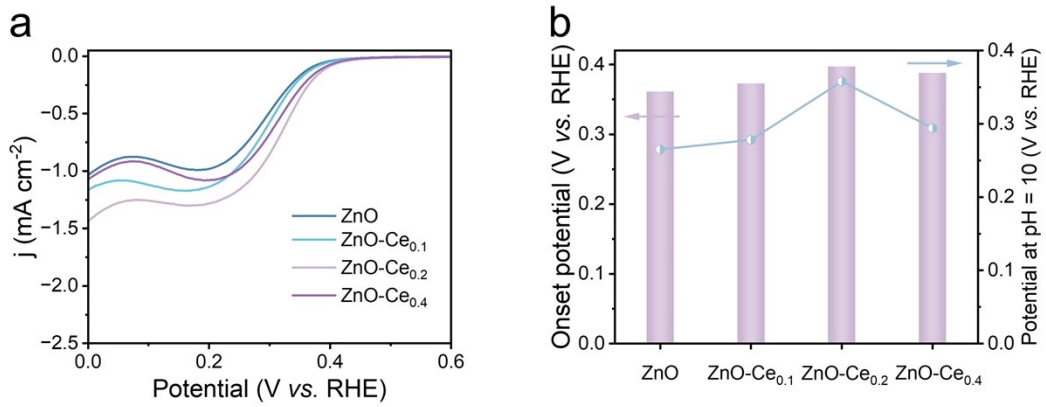

Figure S16 (a) The disk current densities tested by RRDE; (b) The relationship between the onset potential of 2e-ORR and local pH.

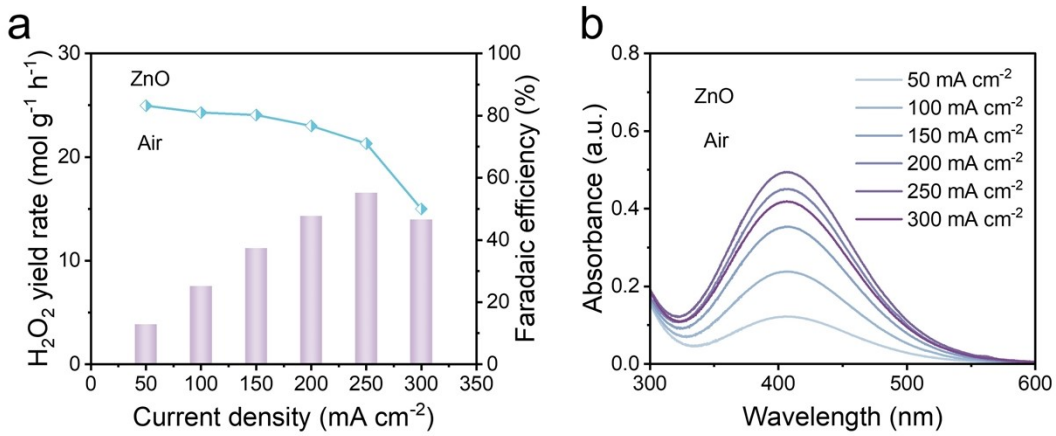

Figure S17 The air-to-H_2O_2 performance of ZnO in flow cell. (a) The H_2O_2 yield rates and Faradaic efficiencies calculated by chronopotentiometry test; (b) The UV-vis spectra under chronopotentiometry test at different current densities.

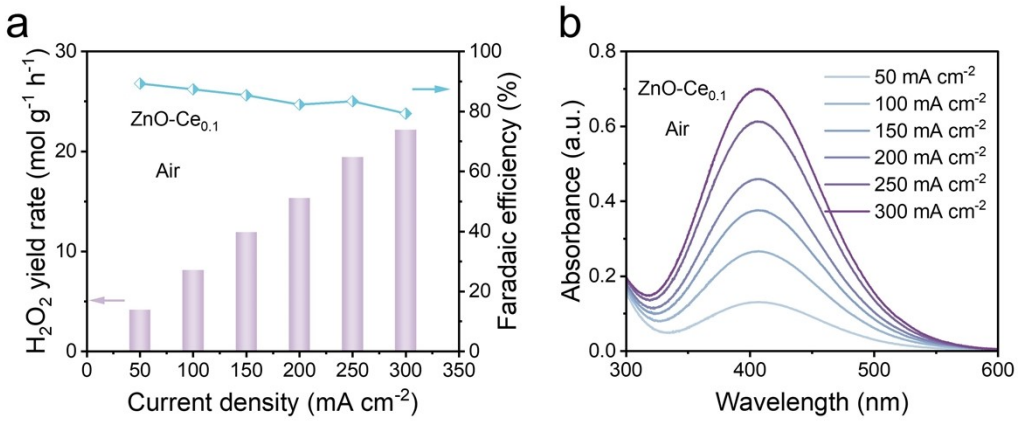

Figure S18 The air-to-H_2O_2 performance of ZnO-$Ce_{0.1}$ in flow cell. (a) The H_2O_2 yield rates and Faradaic efficiencies calculated by chronopotentiometry test; (b) The UV-vis spectra under chronopotentiometry test at different current densities.

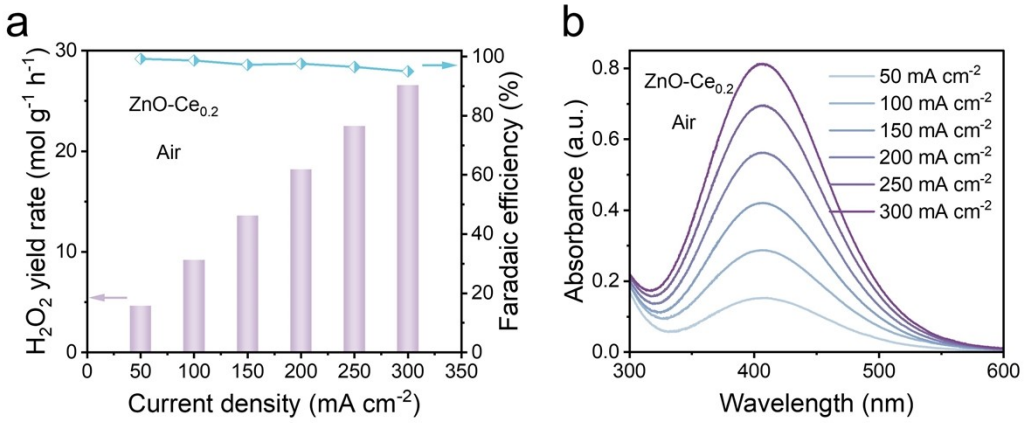

Figure S19 The air-to-H_2O_2 performance of ZnO-$Ce_{0.2}$ in flow cell. (a) The H_2O_2 yield rates and Faradaic efficiencies calculated by chronopotentiometry test; (b) The UV-vis spectra under chronopotentiometry test at different current densities.

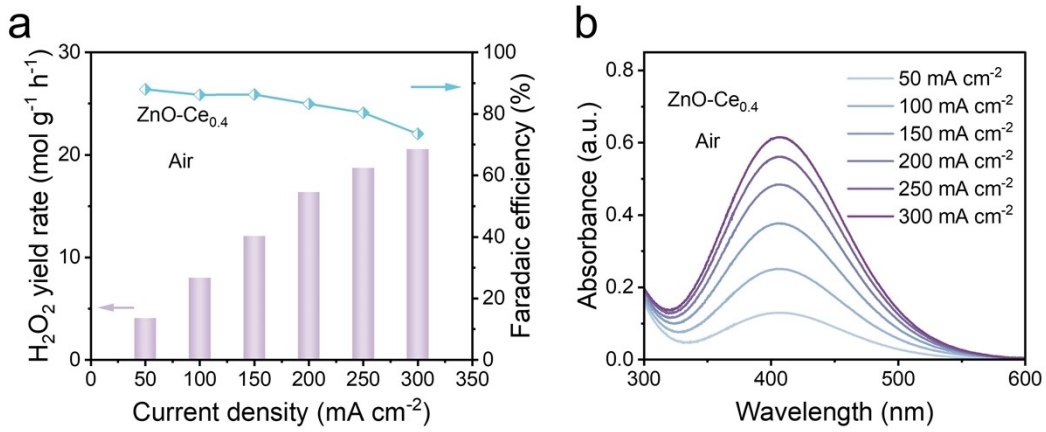

Figure S20 The air-to-H_2O_2 performance of ZnO-$Ce_{0.4}$ in flow cell. (a) The H_2O_2 yield rates and Faradaic efficiencies calculated by chronopotentiometry test; (b) The UV-vis spectra under chronopotentiometry test at different current densities.

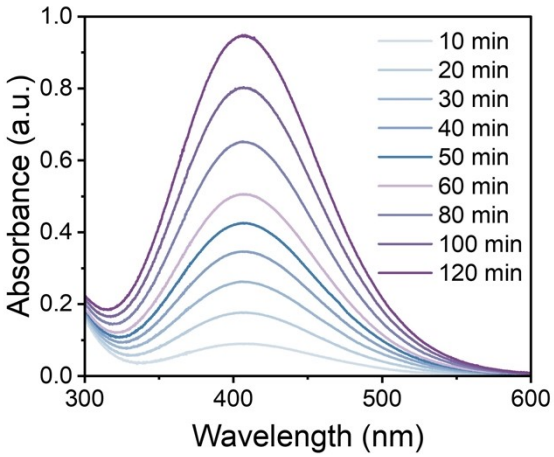

Figure S21 The corresponding UV-vis spectra of the cumulative H_2O_2 concentration of ZnO-$Ce_{0.2}$ electrode.

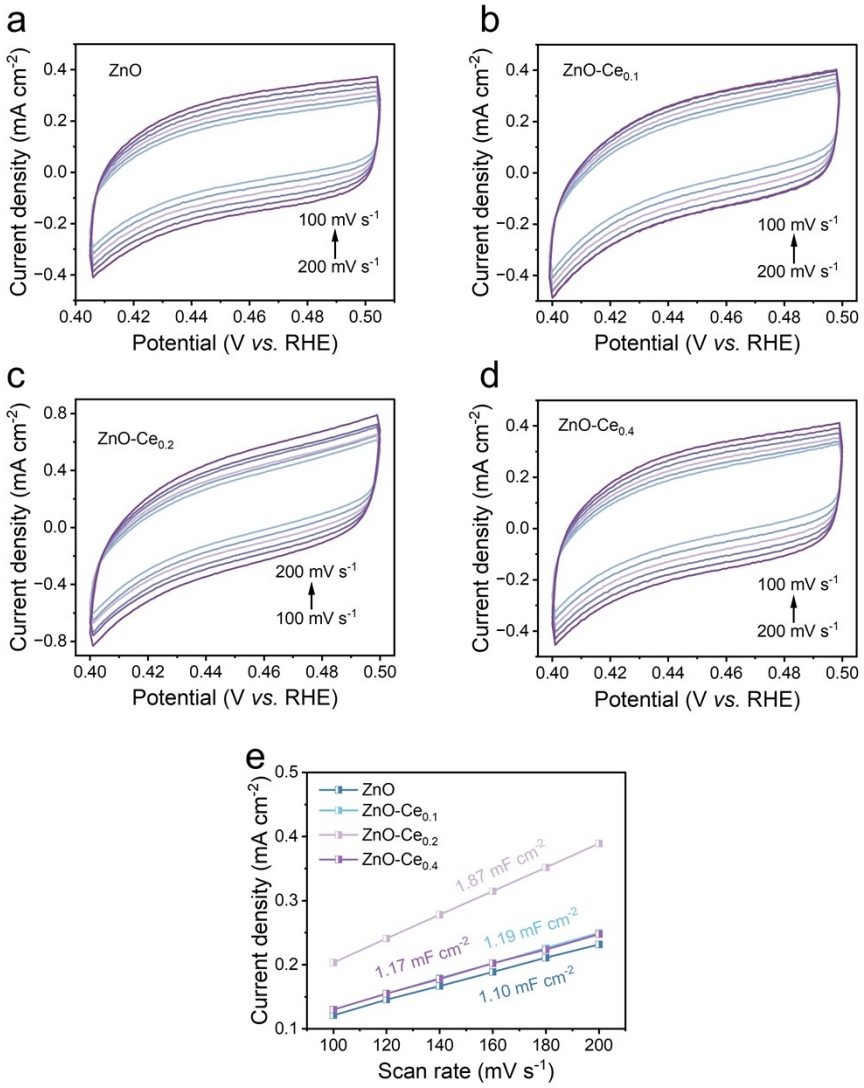

Figure S22 CVs measured at different scan rates from 100 to 200 mV s^{-1}. (a) ZnO; (b) ZnO-$Ce_{0.1}$; (c) ZnO-$Ce_{0.2}$ and ZnO-$Ce_{0.4}$ (d); (e) Capacitance of the electric double layer probed under neutral-pH conditions.

Table S1 The comparison of Faradaic efficiencies (%) of ZnO-$Ce_{0.2}$ with other counterparts under O_2 atmosphere in neutral electrolyte (±5%).

Current density (mA cm^{-2})	**ZnO**	**ZnO-$Ce_{0.1}$**	**ZnO-$Ce_{0.2}$**	**ZnO-$Ce_{0.4}$**
100	77.4	89.0	99.2	86.1
200	82.8	85.1	98.4	84.8
400	77.1	86.2	96.9	82.3
600	70.9	85.1	97.1	82.8

Table S2 The comparison of H_2O_2 yield rates (mol g_{cat}^{-1} h^{-1}) of ZnO-$Ce_{0.2}$ with other counterparts under O_2 atmosphere in neutral electrolyte (±5%).

Current density (mA cm^{-2})	**ZnO**	**ZnO-$Ce_{0.1}$**	**ZnO-$Ce_{0.2}$**	**ZnO-$Ce_{0.4}$**
100	7.22	8.29	9.25	8.03
200	15.45	15.87	18.35	15.82
400	28.74	32.07	36.12	30.69
600	39.65	47.62	54.29	46.35

Table S3 The comparison of Faradaic efficiencies (%) of ZnO-$Ce_{0.2}$ with other counterparts under air atmosphere in neutral electrolyte (±5%).

Current density (mA cm^{-2})	**ZnO**	**ZnO-$Ce_{0.1}$**	**ZnO-$Ce_{0.2}$**	**ZnO-$Ce_{0.4}$**
50	83.2	89.3	99.2	88.0
100	81.0	87.4	98.7	86.2
150	80.2	85.4	97.2	86.3
200	76.7	82.3	97.6	83.3
250	71.0	83.4	96.5	80.4
300	50.0	79.3	95.0	73.5

Table S4 The comparison of H_2O_2 yield rates (mol g_{cat}^{-1} h^{-1}) of ZnO-$Ce_{0.2}$ with other counterparts under air atmosphere in neutral electrolyte (±5%).

Current density (mA cm^{-2})	**ZnO**	**ZnO-$Ce_{0.1}$**	**ZnO-$Ce_{0.2}$**	**ZnO-$Ce_{0.4}$**
50	3.87	4.16	4.63	4.09
100	7.54	8.14	9.20	8.03
150	11.22	11.93	13.59	12.07
200	14.31	15.34	18.20	16.36
250	16.55	19.44	22.49	18.73
300	13.97	22.18	26.56	20.55

Table S5 The comparison of ZnO-$Ce_{0.2}$ with state-of-the-art electrocatalysts towards $2e^-$ ORR in neutral electrolyte.

Catalyst	Atmosphere	Yield (mol g_{cat}^{-1} h^{-1})	Faradaic efficiency (%)	Current density (mA cm^{-2})	Reference
ZnO-$Ce_{0.2}$	O_2	54.29	88.7	600	This work
	Air	26.56	90.9	300	
NC@700 [8]	O_2	16.8	95.8	71	Adv. Funct. Mater. 2024, 34, 2411457
Co@S-1 [9]	O_2	11.56	96	129	Angew. Chem. Int. Ed. 2025, 64, e202506390
Ni-BTA [10]	O_2	13.5	80	100	Nat. Commun. 16 (2025) 4050
In-N_2O_2-P-mC [11]	O_2	22.54	95	250	Angew. Chem. Int. Ed. 2025, 64, e202500177
ER-ZnO [12]	Air	24.4	89.3	300	Nat. Commun. 15 (2024) 4157
N, O-$CNS_{0.5}$ [13]	O_2	6.71	90	100	Adv. Energy Mater. 2024, 14,

					2304418
Pd/MCS-8 [14]	O_2	15.77	88.7	245	Angew. Chem. Int. Ed. 2024, 63, e202403023
Ni-TCPP(Co) [15]	O_2	18.0	85	115	Angew. Chem. Int. Ed. 2024, 63, e202408500
CBNO [16]	O_2	13.4	93	150	Angew. Chem. Int. Ed. 2024, 63, e202317267
L-ZnO [17]	O_2	45.89	98	1000	Energy Environ. Sci., 2023,16, 3363–3372

Supporting Reference

1. B.-H. Lee, H. Shin, A. S. Rasouli, et al., *Nat. Catal.*, 2023, **6**, 234−243.
2. G. V. Fortunato, A. Gunnarson, H. Hosseini, et al., *Adv. Funct. Mater.*, 2026, **36**, e16600.
3. Q. Li, Z. Nie, W. Wu, et al., *Adv. Mater.*, 2025, **37**, 2412039.
4. Q. Yang, W. Xu, S. Gong, et al., *Nat. Commun.*, 2020, **11**, 5478.
5. J. Guo, Y. Zheng, Z. Hu, et al., *Nat. Energy*, 2023, **8**, 264–272.
6. B. Xia, J. Du, M. Li, et al., *Adv. Mater.*, 2024, **36**, 2401641.
7. Y. Yokoyama, K. Miyazaki, Y. Kondo, et al., *Chem. Lett.* 2020, **49**, 195.
8. H. Xie, J. Fu, J. Liu, et al., *Adv. Funct. Mater.*, 2024, **34**, 2411457.
9. G. Yu, Y. Jin, Y. Zhou, et al., *Angew. Chem. Int. Ed.*, 2025, **64**, e202506390.
10. Z. Sang, Y. Qiao, R. Chen, et al., *Nat. Commun.*, 2025, **16**, 4050.
11. C. Qi, W. Bao, J. Xu, et al., *Angew. Chem. Int. Ed.*, 2025, **64**, e202500177.
12. Q. Huang, B. Xia, M. Li, et al., *Nat. Commun.*, 2024, **15**, 4157.
13. L. Jing, Q. Tian, W. Wang, et al., *Adv. Energy Mater.*, 2024, **14**, 2304418.
14. L. Jing, W. Wang, Q. Tian, et al., *Angew. Chem. Int. Ed.*, 2024, **63**, e202403023.
15. Z. Li, J. Jia, Z. Sang, et al., *Angew. Chem. Int. Ed.*, 2024, **63**, e202408500.
16. Z. Song, X. Chi, S. Dong, et al., *Angew. Chem. Int. Ed.*, 2024, **63**, e202317267.
17. S. Ding, B. Xia, M. Li, et al., *Energy Environ. Sci.*, 2023, **16**, 3363-3372.